



This open access document is posted as a preprint in the Beilstein Archives at <https://doi.org/10.3762/bxiv.2025.26.v1> and is considered to be an early communication for feedback before peer review. Before citing this document, please check if a final, peer-reviewed version has been published.

This document is not formatted, has not undergone copyediting or typesetting, and may contain errors, unsubstantiated scientific claims or preliminary data.

Preprint Title Ultrathin water layers on mannosylated gold nanoparticles

Authors Maiara A. Iriarte Alonso, Jorge H. Melillo, Silvina Cerveny, Yujin Tong and Alexander M. Bittner

Publication Date 23 Apr. 2025

Article Type Full Research Paper

Supporting Information File 1 250422supp_Iriarte.doc; 868.0 KB

ORCID® IDs Jorge H. Melillo - <https://orcid.org/0000-0001-7642-0368>; Silvina Cerveny - <https://orcid.org/0000-0001-7727-8156>; Alexander M. Bittner - <https://orcid.org/0000-0003-4815-2444>



License and Terms: This document is copyright 2025 the Author(s); licensee Beilstein-Institut.

This is an open access work under the terms of the Creative Commons Attribution License (<https://creativecommons.org/licenses/by/4.0>). Please note that the reuse, redistribution and reproduction in particular requires that the author(s) and source are credited and that individual graphics may be subject to special legal provisions.

The license is subject to the Beilstein Archives terms and conditions: <https://www.beilstein-archives.org/xiv/terms>.

The definitive version of this work can be found at <https://doi.org/10.3762/bxiv.2025.26.v1>

Ultrathin water layers on mannosylated gold nanoparticles

Maiara A. Iriarte Alonso¹, Jorge H. Melillo^{2,3}, Silvina Cerveny^{2,3}, Yujin Tong^{4,5}, and Alexander M. Bittner^{*1,6}

¹ CIC nanoGUNE (BRTA), Donostia, Spain

² Centro de Fisica de Materiales (CFM-MPC, CSIC-UPV/EHU) Donostia, Spain

³ Donostia International Physics Center (DIPC), Donostia, Spain

⁴ Fritz Haber Inst. der Max Planck Ges., Berlin, Germany

⁵ Abt. Physik, Univ. Duisburg, Germany

⁶ Ikerbasque Basque Foundation for Science, Bilbao, Spain

Email: Alexander M. Bittner, a.bittner@nanogune.eu

Abstract

We investigated the effect of air humidity on two gold nanoparticle systems, one functionalized by an oligo ethylene glycol ligand, and one functionalized by a mixture of the same with a dimannoside ligand. The dimannoside on a gold particle was chosen to mimic the shape and surface chemistry of viral “spike” proteins. We characterized the particles by electron microscopy, dynamic light scattering, and infrared spectroscopy. We probed particles adsorbed on hydrophilic and hydrophobic surfaces with atomic force microscopy (AFM) and vibrational sum frequency generation (VSFG) spectroscopy, both operated under variable air humidity. For AFM, we additionally tested hydrophilic and hydrophobic tips. While VSFG indicated preferential hydration of the dimannoside and proved conformational changes in the organic ligands, AFM provided sub-nm changes in particle topography due to water adsorption. In general, the dimannoside nanoparticles condense ultrathin water layers upon humidity increase. In contrast, we found that the water adsorption on the oligo ethylene glycol particles depends little on humidity. Our insights into structural changes on glyconanoparticles and the hydration properties of glycosylated particles are of application value for biosensors and help model the transmission of airborne viruses, such as influenza.

Keywords

Water; wetting; AFM; sum frequency generation spectroscopy; nanoparticles; viruses; hydrophobicity; hydrophilicity; humidity

Introduction

Gold nanoparticles (AuNPs) are a staple in biomedical and biophysical research [1,2] for almost a century [3]. They are investigated, e.g., for drug delivery [4], but they are also parts of actual products, e.g. of sensors [5]. All this is based on the ease of synthesis, chemical stability, size tuneability, and unique optical properties [6]. The extreme dependence of the properties on particle size and shape has been demonstrated for particle sizes in the 1-100 nm range and on biological interfaces [7]. Limited biocompatibility and high tendency to aggregate in solution inspired new mechanisms of particle biofunctionalization with proteins, lipids, or carbohydrates. Coupling carbohydrates to AuNPs provides particle stability and biocompatibility and allows for studying carbohydrate-mediated interactions and designing novel carbohydrate-based antiviral agents [8,9]. From a molecular point of view, glyconanoparticles are water soluble gold nanoclusters with a three-dimensional carbohydrate display, which defines their biological function [10], with a small core size, of globular shape, and chemically well-defined composition. Proof of concept studies have demonstrated the vast potential of glyconanoparticles for glyconanotechnology in solution. However, potential changes of “glycoclusters” [2] in dry or humid environments are not well known, although there are many examples, e.g. sensors that use antibodies (glycosylated proteins) linked to AuNPs, such as the now very

established SARS-CoV-2 antigen tests [5]. While practical questions around storage conditions and lifetimes call for tests in a realistic environment, the scientific bases are assumptions and analogies to chemically similar systems, rather than data.

Several authors have synthesized and investigated (di)mannoside-coated AuNPs. While there are multiple applications [4], such NPs can also be seen as very crude models of viral “spikes”, which are crucial for virus “survival” during transmission [11,12]. For many, especially mammalian viruses, transmission is in an aqueous environment (e.g. Dengue [13] and Ebola [14]), and air humidity does not play any direct role. In contrast, it strongly affects the transmission of influenza [11,12,15] or SARS-CoV-2 [14] via aerosols. These viruses are enveloped (by glycosylated lipid bilayers) and display very large multimers of nanoscale glycoproteins (“spikes”), which control virus attachment and fusion to the host cells [16]. Glycosylation, often with mannosides [17], is essential to infection. Complete dryness is certainly detrimental (lipid bilayers ultimately collapse). Still, how such virus surfaces are preserved in low humidity conditions is unknown, as is typical for airborne transmission in Northern Hemisphere winters [18]. We believe that a glycosylated AuNP can provide a simplified model of a viral “spike”, whenever the virus is very densely coated, e.g. influenza by hemagglutinin [18,19]. Although the shape cannot be identical (hemagglutinin is roughly a triangular 7 nm prism of 15 nm length), the size is in the typical NP range, and a dense coating with oligomannoside should mimic surface physics. In the same arguments, we note that the adsorption of AuNPs on surfaces would mimic the survival of adsorbed viruses, which can either be transmitted mechanically or again become airborne. In any case, the role of air humidity for adsorbed viruses is poorly documented, and its influence on transmission physics is not known.

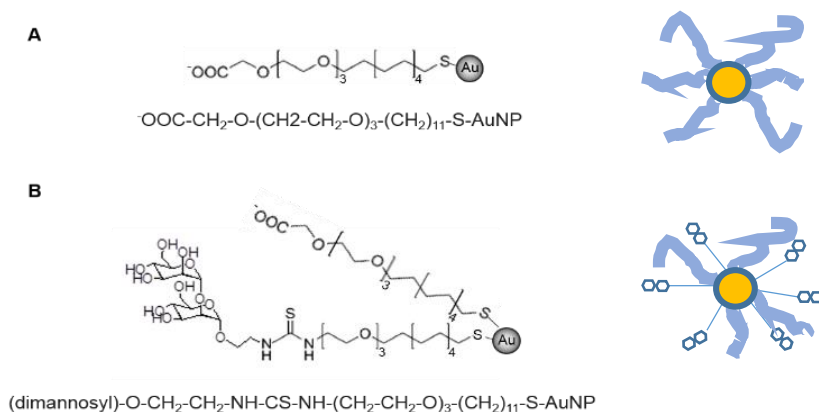


Figure 1. Structures of gold nanoparticles used in this work. (A) PEG AuNPs were obtained in the presence of carboxyl PEG thiol. (B) dimanno-AuNPs were covered with 50 % of dimannoside and 50 % of carboxyl. Note that in (A) and (B) the linear structure of the particles is displayed below the structural scheme. In (B) only the dimannoside is displayed. The yellow circles represent the gold core, the light blue lines the PEG ligand; the thin lines the PEGylated ligand terminated by dimannose residues (two hexagons).

We chose as models dimannoside gold nanoparticles (dimanno-AuNPs) [6] linked to a thiourea PEG thiol chain; the particles also feature COOH-terminated PEG chains (**Figure 1**). We used a typical standard PEG coating on AuNPs, again with COOH termini (PEG AuNPs) for comparison. Here and in the following, we use the established term “polyethylene glycol” (PEG) to designate our relatively short oligo ethylene glycol

chains. The particles were first characterized by dynamic light scattering (DLS) and zeta potential (ZP) measurements in solution, and by scanning electron microscopy (SEM) and scanning transmission electron microscopy (STEM) in vacuum. Samples were adsorbed on flat inorganic surfaces, usually modified with organic layers, and probed by Fourier-transform infrared spectroscopy (FTIR), vibrational sum frequency generation (VSFG), and atomic force microscopy (AFM). For VSFG and AFM, we systematically varied the relative air humidity (RH).

DLS and ZP yield particle size and stability in solution, regarding hydrodynamic diameter and NP surface charge, respectively. Spectroscopy techniques were used to analyze the chemical composition of the organic ligands locally. We used FTIR for the molecular fingerprint infrared region to find the characteristic peaks of the organic layers. In contrast, VSFG was applied to obtain interface-sensitive information on CH and OH bonds at the AuNP/air interface, under hydration and dehydration. We also used a deuterated water (D₂O) atmosphere to distinguish the mannosyl hydroxyl groups from adsorbed and absorbed water.

We achieved detailed spatial characterization by SEM, to measure size and shape, and to detect aggregation upon adsorption on surfaces of different hydrophilicity (see Suppl. Info. S1). We used heavy metal staining in STEM on the nm scale, to distinguish the organic ligand shell from the gold core. The main method, however, was “noncontact” (AC mode) AFM. Its advantage lies in obtaining a very detailed surface topography, i.e., that is a height image. This also includes adsorbed water layers on the sample, which differ from the adsorption on the surface, such that height variations taking place only on the sample are correlated with air humidity [20]. These ideas are inspired by previous works of Verdaguer et al. [20,21] and Chiantia et al. [18].

Ultrathin water layers are extremely delicate, and there is a risk of over-interpreting height information. Indeed, experiments with soft matter in ambient humidity usually create a thin film of water covering the tip and the sample. A mechanical capillary water neck is formed in hydrophilic systems when the AFM tip comes close to the sample surface [22]. In unfavorable cases, this can result in apparent heights up to four times larger than the actual values [23]. Experimentally, this issue can be reversed by different approaches. First, the height measurements can be achieved at set point ranges and working distances where only attractive regimes in the amplitude-distance curves are accessed. Second, tips with different hydrophilicity complement topographic information with accurate height determination. Third, the same is true for surfaces; self-assembled monolayers (SAMs) of silanes are well suited to assess the water layer contribution in AFM measurements [24]. They form stable and well-defined organic layers on oxides, e.g. on oxidized silicon wafers or glass, where surface charge and hydrophilicity are controlled by selecting the appropriate end groups. We combined all the methods mentioned to carry out AFM at variable relative humidity (RH) levels in our AuNP systems. Specific care was taken for height measurements, as demonstrated by amplitude-distance curves and statistical analysis (t-tests). We added experiments with deuterated water analogous to the mentioned VSFG tests.

Results

The dimanno-AuNPs consist of functionalized AuNPs with a mixture of dimannoside ligand and a PEGylated ligand. The PEG AuNPs were functionalized only with the

PEGylated component; they can be seen as a precursor, and we used them as negative controls.

Particle size and shape

Particle size and stability in an aqueous solution were characterized by DLS and ZP, while size and morphology in completely dry conditions were measured by electron microscopy.

DLS yields a hydrodynamic diameter of the PEG AuNPs of 67.7 ± 9.4 nm and a polydispersity index (PDI) of 0.35. However, the size distribution (**Figure 2**) reaches a maximum at (41.1 ± 4.2) nm. These results indicate that the sample was slightly polydisperse. Hence, a small number of multimers of the NPs is present in the solution. In contrast, the size average of the dimanno-AuNPs was (30.4 ± 1.1) nm (PDI 0.29) with a peak at (16.8 ± 0.9) nm. This indicates that the dimannoside coating results in reduced nanoparticle aggregation.

In both cases, the NP surface charge in water at pH ~ 7 was ~ 20 mV. The isoelectric point of carboxylate PEG capped particles is ~ 2.5 , so around pH 7 they should exhibit a negative ZP. This is also compatible with a low carboxylate content, as citrate capped AuNPs (with a higher concentration of carboxylate) exhibit a lower ZP (~ 45 mV) at the same pH [1].

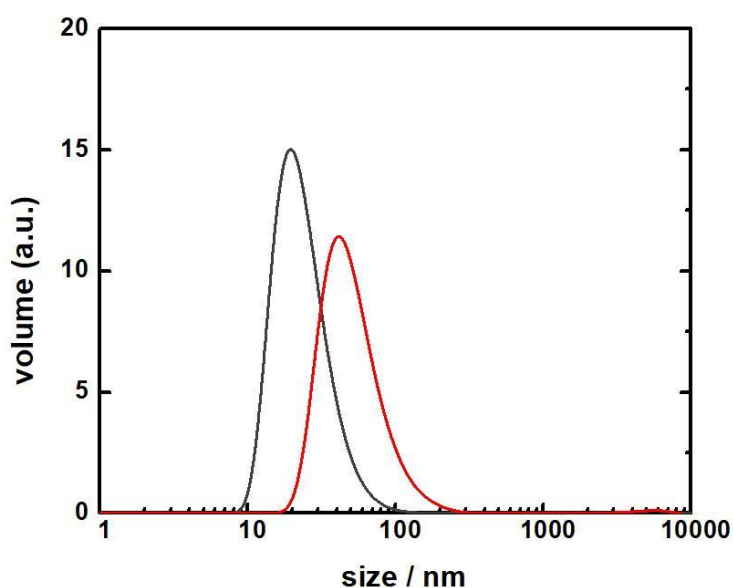


Figure 2: Distribution of hydrodynamic diameters of dimanno-AuNP (black) and PEG AuNP (red) solutions, obtained by DLS.

To obtain a clearer view of the size distribution, we used SEM to evaluate particle sizes and morphologies in high vacuum (i.e. for completely dried samples). By adjusting a Gaussian fitting to the histograms (**Figure 3**), the diameter of the particles adsorbed on APDMES silicon was estimated. The dimanno-AuNPs exhibited a mean size of (14.8 ± 1.6) nm (**Figure 3-A and 3-C**), and the size of the PEG AuNPs was (14.3 ± 1.5) nm (**Figure 3-B and 3-D**).

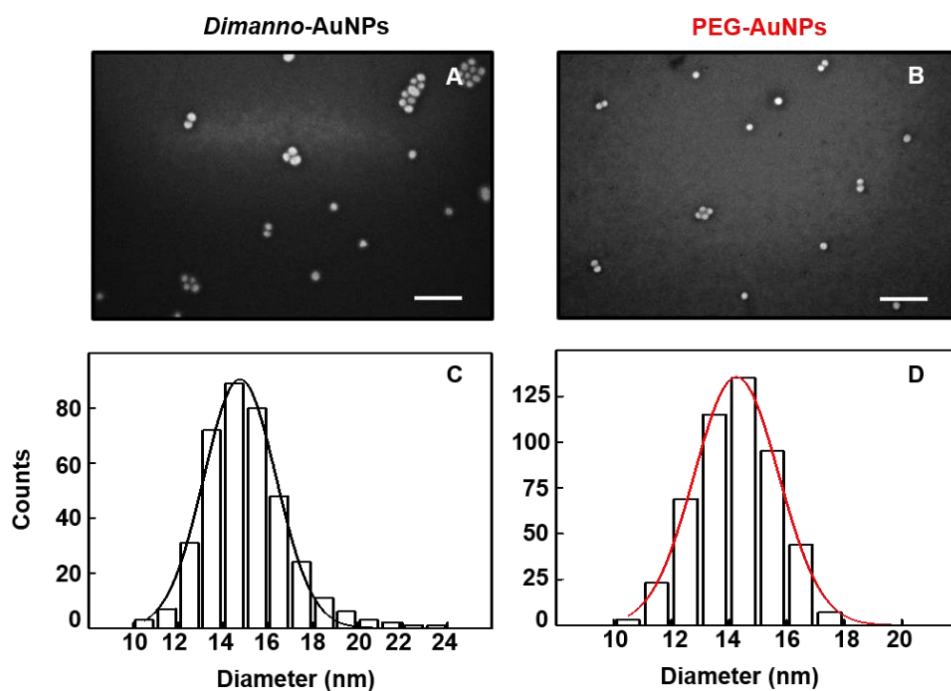


Figure 3: SEM images of dimanno-AuNPs and PEG AuNPs adsorbed to a hydrophilic surface. (A) Dimanno-AuNPs, (B) PEG AuNPs (scale bars 100 nm). (C and D) Particle size histograms (diameter) from (A and B), respectively.

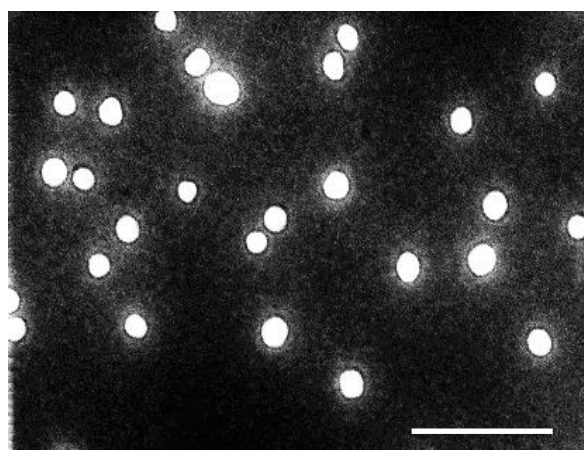


Figure 4: STEM image of negatively stained dimanno-AuNPs (scale bar 100 nm). The gold cores appear bright, the carbon grid background is dark, and the organic layer appears as grey halo.

The organic layers from PEG and dimannoside are transparent to electrons in SEM (only the gold cores were observed as bright features). We recorded STEM images of dimanno-AuNPs deposited on a carbon coated TEM grid to visualize the layer. We employed uranyl as a stain, a soluble heavy metal cation, which attaches to the hydrophilic parts of the organic coating, providing good contrast [25]. The STEM images in dark field mode (imaging scattered electrons) show the gold cores as bright structures, whereas the thin organic layers are dark. The carbon grid yields practically no scattering and appears essentially black, such that both the core and shell of the particles can be distinguished (**Figure 4**). The estimated organic layer thickness is 1.5

nm, as obtained by subtraction of the total radius of the negatively stained particles and the radius of the gold cores.

Analysis of the chemical groups

The nature of the coating layer of (PEG AuNPs and dimanno-AuNPs) was characterized by FTIR (only in dry nitrogen) and VSFG at variable humidity. We discuss details of the FTIR spectra in the Suppl. Info. S2, including the origin of the different bands. Here, we mention that the PEG AuNPs spectra exhibit only a trace of O-H stretching bands, in stark contrast to dimanno-AuNPs. It is well known that sugars are very difficult to dry completely, so related bands are easily found in many carbohydrates (see Suppl. Info. S2).

For the VSFG, the ssp polarized spectra were obtained by adding a droplet of H₂O or D₂O on the dried samples and subsequent evaporation (G-A and G-B). The VSFG spectra focus only on the high frequency region. The vibrational bands are superimposed on a very broad signal from bulk gold, quasi-constant after normalization (like FTIR). In contrast to FTIR, the bands stem only from vibrations at interfaces, hence from the NP surface in contact with air. Additionally, highly symmetric vibrations are forbidden (with very low or zero intensities) [26].

The PEG signals correspond, as expected, quite well to the infrared spectrum, with a strong peak at 2880 cm⁻¹. This feature points to a lack of local order, which should be based on disorder of the PEG chain (ordered alkyl chains, for example, yield no signal from CH₂). Moreover, the peak is unusually broad, possibly due to the complex shape of the disordered PEG alkyl chain. However, the disorder is only present in each chain; altogether, the C H stretching vibrations must have a preferred orientation with respect to the gold surface. In other words, the nanoparticle has a non-centrosymmetric environment, which can simply be the presence of the gold surface. The noise-like feature at ~3400 cm⁻¹ is assigned to hydrogen-bonded water, as features above 3600 cm⁻¹ should indicate non-hydrogen-bonded water. This is proof that water is adsorbed on the PEG AuNPs. A quantification is not possible; however, there cannot be more than a few monolayers, otherwise the band would completely dominate the spectrum. This is also in agreement with the absence of the band in FTIR. Hence, the hydrophilic PEG chain binds water, but can easily be dried, while the last traces remain. This is similar to a strongly bound water (mono)layer on biomolecules.

The dimanno-AuNPs, under the same conditions, exhibit a very different spectrum: The C H stretching bands at 2850 cm⁻¹ and 2920 cm⁻¹ (see also FTIR) are "negative", i.e. the background VSFG signal is diminished. The frequency only slightly shifts from that of CH₂ groups in alkyl and PEG chains. The "dip"-like features should be due to the interference effect between the resonant and the non-resonant signal. The different features of PEG-Au and dimanno-Au may be due either to the other dipole orientation of the CH group between the two samples [27], or to the charges of the molecules being opposite [28]. The latter seems unlikely since the isoelectric points of the two samples are similar.

By the symmetry rules and the ssp-polarization, one can deduce that the CH₂ groups are again oriented, but different from those in the PEG AuNPs. This shows directly that the dimannoside strongly affects the PEG and alkyl chain conformation. We can

exclude disorder and propose a stretched-out geometry based on the relatively narrow bands. The dimannoside must be covered by water, and indeed, a peak assigned to liquid water is present. Water on the dimannoside can adsorb in a multitude of orientations. This averaging results in a low signal. **Figure 5** provides a sketch of the principal ideas.

VSG experiments were repeated after exposure to D₂O. The original idea of using D₂O was to distinguish the hydroxyl groups of the sugar molecules from those of adsorbed/absorbed water. However, the surface hydroxyl groups of amorphous sugar may also be subject to H-D exchange [29]. Nevertheless, **Figure 5-B** indicates that the H₂O molecules of the top water layer can exchange back under the experimental conditions. The time for the isotope exchange is extremely long: days or even months [29]. Deuteration usually assesses the exchange capability of the hydroxyl groups in infrared frequencies between 3100 and 3700 cm⁻¹. Also, the slower structural dynamics at the air/D₂O interface allow better visualization of signals related to the air/H₂O interface on the particles and enable finding whether there are ordered water molecules at the sample surface.

In this experiment, the D₂O exposure time of 30 minutes is not sufficient to exchange the H in the dimannose OH groups [29]. However, due to its large excess, it should replace the thin layers of adsorbed water. **Figure 5-B** shows that this is indeed the case, the CH region is practically unchanged, while the 3400 cm⁻¹ signals are barely present. Note that the OD stretch in liquid D₂O is shifted to 2500 cm⁻¹. In this way, the model of thin adsorbed water layers is bolstered, also showing the strongly hydrophilic nature of both PEG AuNPs and dimanno-AuNPs.

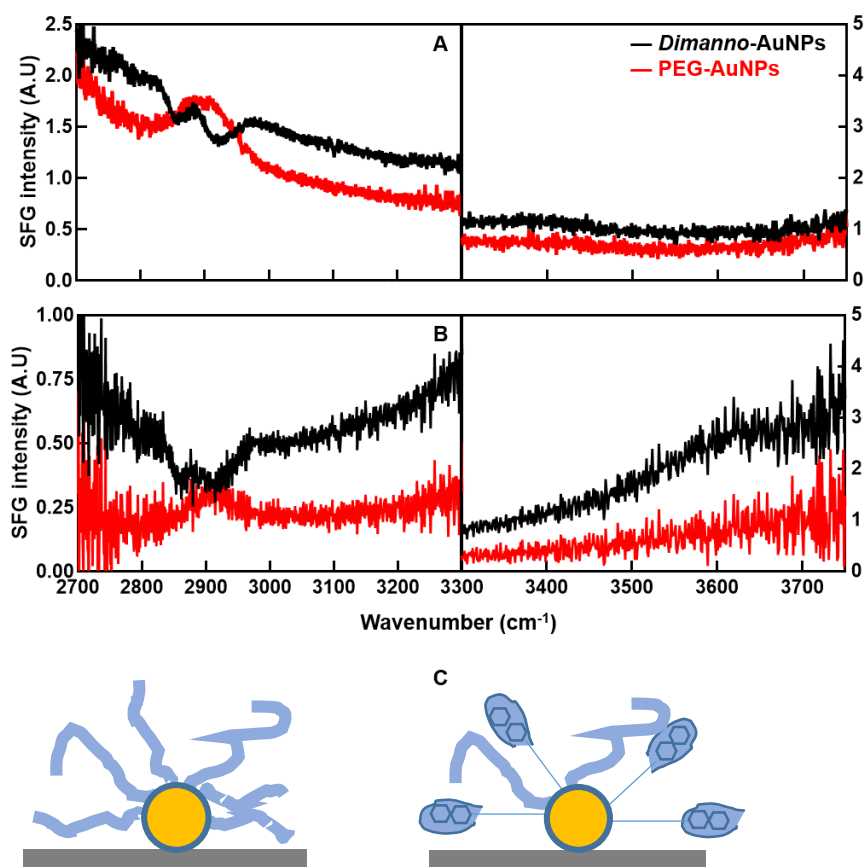


Figure 5: Normalized VSFG spectra in CH and OH region of dimanno-AuNPs and PEG AuNPs on gold surface, ssp (s VSFG, s vis, p IR) polarization combinations. (A) VSFG spectra in H₂O. (B) VSFG spectra in D₂O. The black line represents the VSFG spectra of dimanno-AuNPs; the red line represents the VSFG spectra of PEG AuNPs. Note the different y-axis scale. (C) Model of the proposed conformations of dimanno-AuNPs and PEG AuNPs. PEG AuNPs (left) show little order in the PEG chains. Dimanno-AuNPs (right) show a stretched-out geometry provided by the dimannose residues (organic layers not drawn to scale). The yellow circles represent the gold core; the flexible light blue line represent the PEG ligand; the rigid line represent the PEGylated ligand ordered by the presence of dimannose residues (two hexagons), surrounded by water (droplet-like blue areas).

Adsorption of the particles on hydrophilic and hydrophobic surfaces

We assessed the aggregation tendency of the particles after adsorption with SEM and AFM. To this end, we determined water contact angles. The hydrophilic APDMES silicon gave $66 \pm 3^\circ$. In contrast, on the hydrophobic OTS silicon it was $92 \pm 2^\circ$. Comparison of the two surfaces shows characteristic differences (Figure 6), as known from analogous investigations with tobacco mosaic virus [30] and with surface-layered proteins [24].

The dimanno-AuNPs are homogeneously distributed on APDMES. Consequently, SEM images have low contrast (Figure 6-A). Zooming to the nanoscale, we found a homogenous dispersion of the particles (Figure 6-B). This is supported by AFM topography images at the nanoscale (Figure 6-C). In contrast, PEG AuNPs are not well dispersed, with more agglomerates (see the analogous Figure 6-G, 6-H, 6-J), and particle clusters form microscale islands.

We analyzed adsorption on the hydrophobic OTS with the same procedure (Figure 6-D, 6-E, 6-F and 6-J, 6-K, 6-L). Here, the required drop-casting method resulted in a coffee ring effect [31], as nicely seen in Figures 6-D and 6-J. Local in-homogeneities prevail on areas inside and outside the ring. Generally, we observed here a very small number of NPs and higher agglomeration than on APDMES (Figure 6-E, 6-F, 6-K, 6-L). Like the case on APDMES, PEG AuNPs are less uniformly distributed than dimanno-AuNPs.

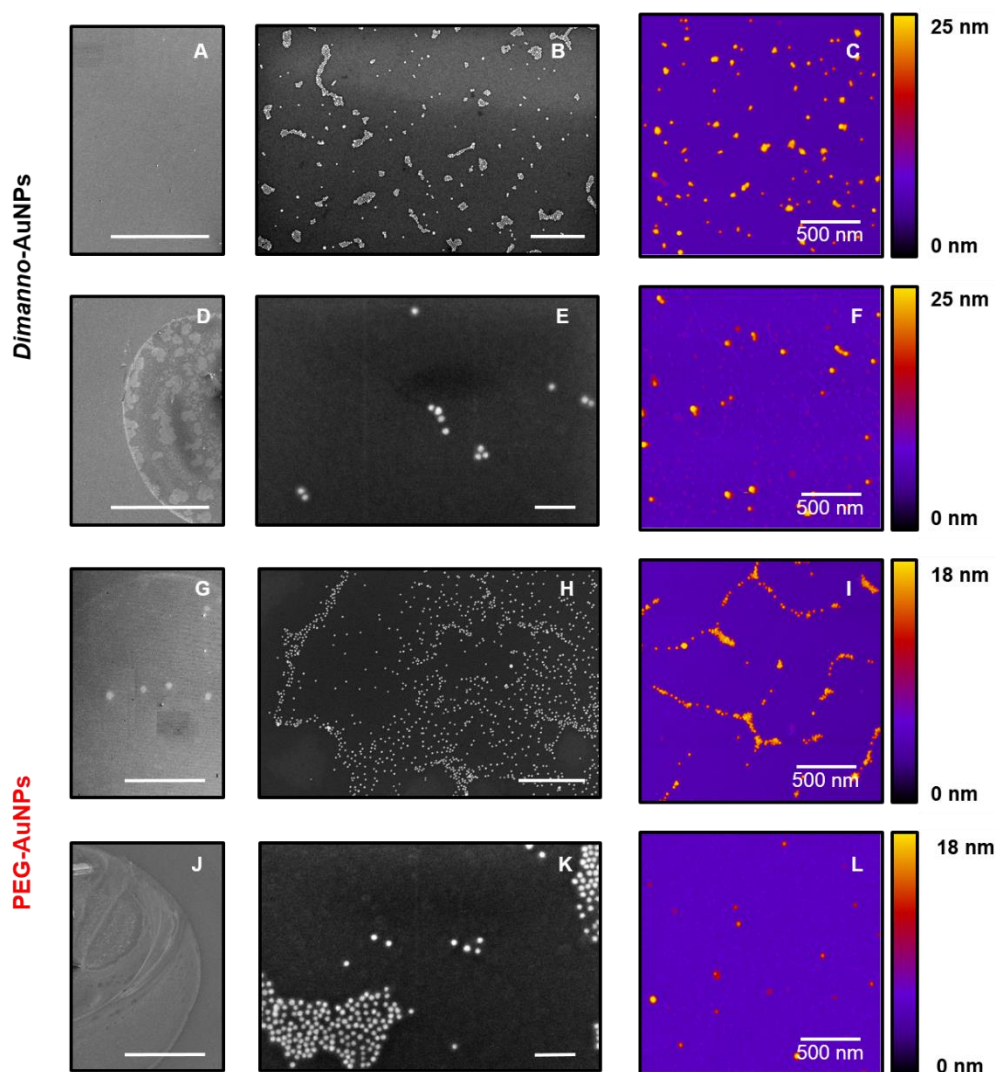


Figure 6: Representative SEM and AFM images of dimanno-AuNPs and PEG AuNPs on hydrophilic and hydrophobic surfaces. (A, B, D, E, G, H, J and K) SEM images. (C, F, I and L) AFM images. (A C) Dimanno-AuNPs adsorbed on hydrophilic APDMES modified wafer. (D F) Dimanno-AuNPs adsorbed on hydrophobic OTS modified wafer. (G I) PEG AuNPs adsorbed on the hydrophilic surface. (J L). PEG AuNPs adsorbed on the hydrophobic surface. Scale bars 400 μm (A, D, G and J), 500 nm (B and H), 100 nm (E and K). The AFM height scale is adjusted to each particle diameter.

Detailed height measurements of adsorbed particles in water vapour

AFM under variable RH was based on three distinct hydration conditions, which we define as 1) “low humidity”, (15 ± 5) % RH, corresponding to desert climate (or very low temperatures); 2) “medium humidity”, (50 ± 5) % RH, which is slightly above the standard comfort value, and 3) “high humidity”, which required overnight sample incubation to reach (90 ± 5) % RH, corresponding to very wet climate or air during precipitation.

In addition, we refer to “hydrophilic conditions” in AFM for hydrophilic surfaces (APDMES silicon) scanned by a silicon tip. We found a vertical resolution (Δz) of 0.04 nm and a surface roughness of 0.16 nm (for scans in the 100 to 1000 nm range).

Amplitude–distance curves (see Suppl. Info. S3) suggest working regimes controlled by long-range attractive forces, both at low and high humidity. Under these conditions, we minimize sample damage, and capillary forces, albeit present, play no significant role.

We imaged randomly selected NPs under the three humidity conditions and analyzed their height profiles. In the following, we focus on selected single particles. For the dimanno-AuNPs, the maximum height, z_{\max} , of the NP in **Figure 7-A** was 15.6 nm at ~15 % RH). We found 15.8 nm, hence no measurable increase, at ~50 % RH (**Figure 7-C**), but 17.7 nm at ~95 % RH (**Figure 7-E**), a 2.1 nm increase. For PEG AuNPs, we chose two particles of 13.3 nm (left) and 12.9 nm (right) (**Figure 7-B**). Here, the z_{\max} decreased upon humidity increment, to 12.4 nm and 11.9 nm (**Figure 7-D**), and finally at high humidity 12.0 nm and 11.9 nm, respectively (**Figure 7-F**). The Suppl. Info. S4 provides additional details.

To increase the statistical accuracy of the experiment, we tested ~500 randomly selected particles under the same humidity conditions (**Figure 8-A and 8-C**, Table 1). The resulting box plots for the hydrophilic conditions correlate well with the analysis on the selected single particles (**Figure 7**, see also related scans in the Suppl. Info. S4): The particle height of (16.7±1.6) nm increases by 0.3 nm under medium, and by 1.6 nm under high humidity. The PEG AuNPs of (13.3 ± 1.0) nm show a slight reduction by 0.3 nm, but only at high humidity, which is within the uncertainty of the experiments.

To prove that the increase in z_{\max} is solely due to the adsorbed water, we repeated the experiments under hydrophobic conditions: We employed OTS silicon surfaces and hydrophobic carbon AFM tips. From this, we exclude that the observed phenomena is specific for the type of surface [32] or based on mechanical contact between tip and surface [22,23,33]. The Δz in ambient conditions was 0.03 nm and the roughness of the OTS on silicon was 0.55 nm for scans between 100 and 1000 nm. In this case, it was not possible to follow the same particles along the different humidity steps due to the instability of the measurement, which did not allow locating the scanned area after changing the humidity level. We recorded ~250 measurements of single particles on random positions (**Figure 8-F and 8-D**, Table 1). The data at variable humidity for dimanno-AuNPs fit well with the observations under hydrophilic conditions, we found an increase in z_{\max} of 1.7 nm from low to high humidity (**Figure 8**). In contrast, the results of the PEG AuNPs under hydrophobic conditions differed slightly from those under hydrophilic conditions, we found an increase of 0.8 nm (**Figure 8**).

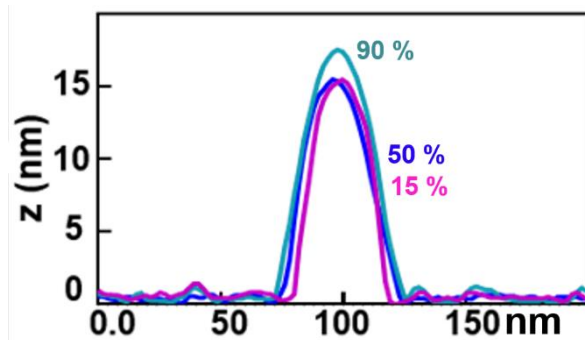
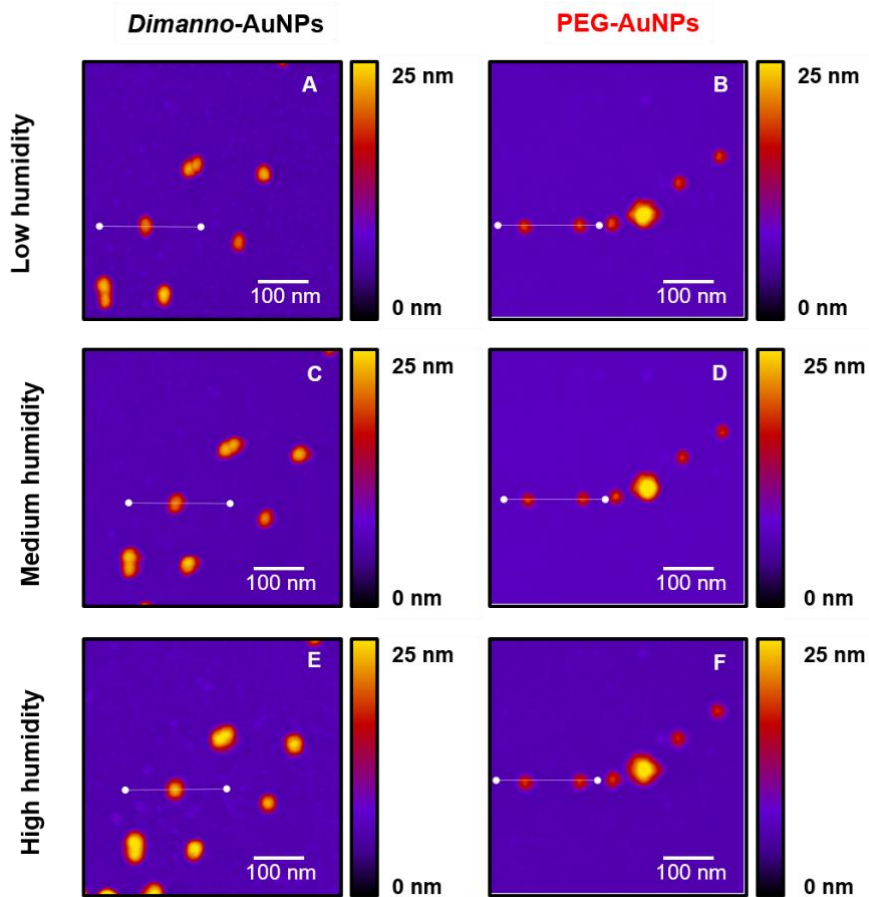


Figure 7: AFM topography of dimanno-AuNPs and PEG AuNPs under hydrophilic conditions (silicon AFM tip, APDMES silicon surface) (A and B) Low humidity (~15 % RH), (C and D) medium (~50 % RH), (E and F) high (~95 % RH). (A,C,E) Dimanno-AuNPs; (B,D,F) PEG AuNPs. Lower panel: Overlay of the three profiles shown in (A,C,E)

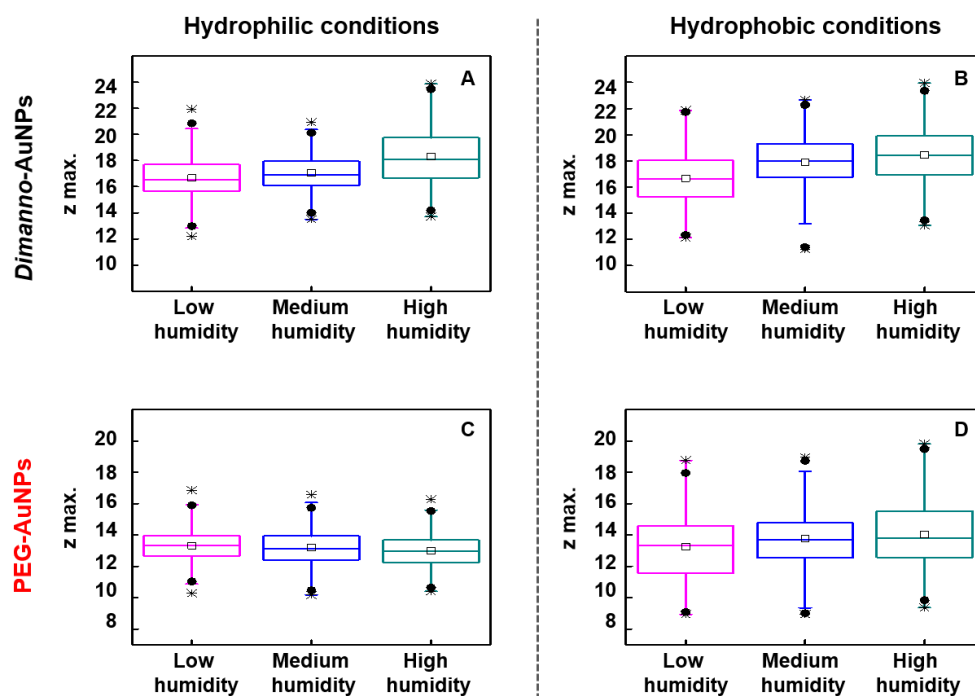


Figure 8: Box plots of AFM heights of dimanno-AuNPs and PEG AuNPs obtained in different humidity levels. AFM data of dimanno-AuNPs under (A) hydrophilic conditions (APDMES surface, silicon tip, ~500 experiments), and (B) hydrophobic conditions (OTS surface, carbon tip, ~250 experiments), and of PEG AuNPs under (C) hydrophilic and (D) hydrophobic conditions, respectively. Magenta boxes refer to low humidity, blue boxes to medium humidity and dark cyan boxes to high humidity. Each box plot shows the interquartile range (from 25 % to 75 %). The extreme of the box represents the 5 % and 95 % quartile, respectively. Middle lines represent the median and the squares of the mean value. Black circles are the 1 % and 99 % quartile, and black stars are the minimum and maximum value.

In addition, in AFM experiments, we used air humidified with D₂O instead of H₂O again on dimanno-AuNPs adsorbed on gold and scanned with a silicon tip (Suppl. Info. S5). Although we expected no difference, this test was required to compare the conditions to those used in the VSFG experiments. Working with D₂O can allow for exploring molecular hydrate structures [29]. Here, we aimed to identify if the increase in the maximum height of single particles was merely driven by the adsorption of water layers on top of the dimannose residues, or by other mechanisms such as swelling, i.e. incorporation of water into the NP shell. As in the previously introduced cases, the particles increased their maximum height when the humidity of the system increased. This was influenced neither by the surface nor by the tip. So, our D₂O data compares well with those under hydrophilic and hydrophobic conditions (Table 1). We evaluated 300 experiments.

Table 1: Maximum heights (Z_{\max}) of individual dimanno- and PEG-AuNPs measured by AFM at different hydration conditions. Results expressed as the mean \pm SD. Uncertainties were obtained from statistical errors. The number n refers to the evaluated AFM scans. We tested the reliability of our Z_{\max} values with a nonparametric Mann-Whitney test (Suppl. Info. S6). For the dimanno-AuNPs, under hydrophilic and hydrophobic conditions and for experiments with deuterated water, we found no significant differences in sample distribution at both low ($p = 0.46$) and high humidity ($p = 0.06$). PEG AuNPs depend on the scanning conditions, but only when comparing hydrophilic and hydrophobic conditions at high humidity ($p < 0.0001$).

Particle	Surface	water vapor	Z_{\max} low humidity (nm)	Z_{\max} medium humidity (nm)	Z_{\max} high humidity (nm)
<i>Dimanno-AuNPs</i>	APDMES/Si, hphilic	H ₂ O	16.7 \pm 1.6 (n=594)	17.0 \pm 1.4 (n=532)	18.3 \pm 2.1 (n=492)
<i>Dimanno-AuNPs</i>	OTS/Si, hphobic	H ₂ O	16.7 \pm 2.0 (n=594)	17.7 \pm 2.3 (n=532)	18.4 \pm 2.2 (n=492)
<i>Dimanno-AuNPs</i>	Gold,hphilic	D ₂ O	16.6 \pm 1.6 (n=300)	17.2 \pm 1.5 (n=300)	17.9 \pm 1.9 (n=300)
PEG-Au NPs	APDMES/Si, hphilic	H ₂ O	13.3 \pm 1.0 (n=505)	13.2 \pm 1.1 (n=495)	13.0 \pm 1.0 (n=499)
PEG-Au NPs	OTS/Si, hphobic	H ₂ O	13.2 \pm 2.1 (n=505)	13.7 \pm 2.0 (n=495)	14.0 \pm 2.2 (n=499)

Discussion

We first discuss the spectroscopic results. FTIR and VSFG confirm the chemical composition of the organic layers (**Figure 1** and 5). The VSFG results additionally give sensitive information on the local ordering of the molecular chains in the ligands. We conclude that the dimannose residues are coupled to the PEG chains, and provide specific ordering properties: Under dry conditions, both PEG and dimannoside bind water. However, the higher hydrophilicity of dimannoside enables a better interaction with water molecules, which remain bound even after dehydration. This is also supported by research on SAMs on gold surfaces, which reveal a more hydrophilic tendency of surfaces functionalized with mannose terminal groups (C₆H₁₂O₆C₅S, contact angle $< 5^\circ$), compared with carboxylic acids (COOHC₁₁S, contact angle $44^\circ \pm 1^\circ$) [34]. Whenever NPs cluster, the steric hindrance effects of the bulky dimanno-AuNPs should additionally create nanoscale "traps" between the NPs. Both effects result in water adsorption that persists even in dry environments.

Focusing now on particle size and assembly, we found no difference between the hydrodynamic size of 16.8 nm (obtained in suspension by DLS) (**Figure 2**) and the AFM height of 16.7 nm (which we here limit to the case of complete dehydration) (Table 1). DLS usually gives higher particle sizes due to the hydration layer [35,36], which slows the diffusion of NPs in aqueous solutions, especially our hydrophilic NPs. We suggest two possible explanations, first, the dimannose residues could be very efficiently packed (with PEG ligands acting as spacers), second, the adsorption of the NPs distorts the ligands between the NP core and the solid surface. The latter effect is well known from adsorbed NPs, where one should consider up to three ligand spaces, ligands between NP and surface, ligands that stretch out parallel to the surface, in contact with it, and free ligands, which are merely attached to the NP.

For the PEG AuNPs, DLS gave an extreme value of 41.1 nm, corresponding to three AFM height values (13.3 nm). We conclude that we here observe particle agglomeration in solution. Previous studies have shown such clusters for PEG AuNPs in solution [37]; their size is strongly reduced by adding albumin. In our case, the addition of dimannose would lead to the case of the dimanno-AuNPs, for which we do find much decreased agglomeration. Generally, nanoparticles produced inside a concentrated carbohydrate solution (more than 40 % of the total aqueous volume) provide a macromolecular crowding environment which diminishes particle interaction [38]. The dimanno-AuNPs used in this research were produced in a solution of ~50 % dimannoside ligand sufficient to decrease the agglomeration tendency. The observed excellent stability of dimanno-AuNPs may be associated with the physical constraint of the dimannoside being present during synthesis, and the strong intra NP hydrogen bonding interactions.

These properties are also reflected in the macroscale structures formed upon adsorption. However, the surface is crucial here, and our hydrophilic APDMES and hydrophobic OTS silanized wafer surfaces (see Suppl. Info. S1) provide two extremes (**Figure 6**). We observed a “coffee ring” drying phenomenon only on OTS. This is related to the competition between the time scales of the liquid evaporation and the particle movement: The solvent evaporates so slowly that particles move over at least mesoscale distances, thus allowing aggregation in the ring [31]. In our research, the deposition protocol may have influenced the observed phenomena. The hydrophilic APDMES favors NP surface interactions with subsequent immobilization. This can be based on multiple hydrogen bonds between the NH_3^+ groups in APDMES and the OH groups in the dimannoside, which immobilizes the NPs long before solvent evaporation. Consequently, in this case, we observed no “coffee ring” effect. The drop-casting method used on the OTS allowed complete evaporation of the droplet. The relatively weak NP surface interactions are now dominated by hydrophobic effects, and inter-NP interactions are favored, while NP movement was faster than evaporation, resulting in the observed “coffee ring” drying.

Mesoscale observations of NP assembly by AFM and SEM complement the results discussed above. The use of hydrophilic and hydrophobic surfaces and also AFM tips allows to distinguish ubiquitous water layers, present on all surfaces, from specific water adsorption on the AU NPs. For the APDMES surface at neutral pH, we expect electrostatic interactions between the NH_3^+ groups and the carboxylate residues on the NPs, and hydrogen bonds. Hence, there are relatively few differences between dimanno-AuNPs and PEG AuNPs, which are related to the particle dispersion in solution. The clustered PEG AuNPs cannot disperse well on a surface, while the single dimanno-AuNPs interact efficiently, indicating that NP-surface interactions dominate in this case over NP-NP interactions. We ascribe this to hydrogen bonds between the (multiple) OH groups in the dimannoside and the amine. This finding compares well with TEM on carbon grids: PEG AuNPs with short or long ethylene glycol chains adsorb in clusters [39], while glycosylated AuNPs are homogeneously dispersed [10].

Our observations of nanoscale hydration by AFM show a general trend to stronger water adsorption on dimanno-AuNPs, as compared to the PEG AuNPs (**Figure 7**). This agrees with AFM hydration studies of sucrose particles, which become liquid above 60% RH [41], hence, the more hydrophilic nature of the dimannose residues is expected. Statistical analysis demonstrates that only the water adsorption on dimanno-AuNPs is independent from the scanning conditions (Table 1 and Suppl. Info. S6). Between hydrophilic and hydrophobic conditions we find only small differences, which

we interpret as quasi-identical ubiquitous water layers on our silanes: Although APDMES would be expected to bind more water than OTS, this increase is smaller than our experimental error.

Considering the size of a water molecule (~0.28 nm) and the typical thickness of hydration layers (~0.6 nm) [21,22,40,42,43], the absolute values of water adsorption on dimanno-AuNPs fit to three to four layers of water (~1.5 nm). STEM found that the organic layer on dimanno-AuNPs is ~1.5 nm (**Figure 4**). Hence, we propose a 100% thickness increase due to water adsorption or absorption, i.e., the water can be present in a layer, adsorbed, but also in between the various dimannoside groups, absorbed. The latter case would correspond to a "swelling" of the AuNP coating, which is agreement with microbalance observations of highly hydrated cellulose films [44], which find 3.6 mol water per cellulose subunit at 97% RH.

Under hydrophobic conditions, PEG AuNPs show a moderate increase in AFM height, corresponding to one water layer, not observed under hydrophilic conditions. It is possible that this is based on reproducibility issues, which are well known for hydrophobic samples. These can be based on irreversible modification of tip or sample, or even both [33]. In this regard, Wet STEM and SEM investigations on PEG AuNPs differ from our data, indicating that particle hydration is independent of the selected surface [21,22,32,45]. However, these studies were performed on particle clusters in crowded environments, which induce collective phenomena [32,45] that are not in our scope.

Conclusions

Gold nanoparticles (AuNPs) have been widely investigated for biomedical applications, like biochemical sensing, imaging or drug delivery systems. The success of these platforms stems from their dispersion in water, stability and biocompatibility in fully hydrated states, as well as in biological fluids. Our investigation shows a novel approach to these particles by testing the hydration properties at different humidity conditions in the air. We characterized AuNPs coated by oligo-ethylene glycol (PEG) and dimannoside with a multi-method approach (VSFG, FTIR, DLS, ZP, SEM, STEM, AFM). We proved that various properties, mainly those of the adsorbed dimanno-AuNPs, depend on environmental conditions, specifically humidity and the hydrophilicity of the adsorption surface.

Our spectroscopic investigations verify the known chemical properties. With VSFG under controlled humidity, we found ordering phenomena in ligand chains, which we attribute to forces exerted by hydrated dimannoside. Such an ordering is absent in conventional PEG ligands. Our observations of nanoscale hydration by AFM in a humidity chamber show a general trend of stronger water adsorption on dimanno-AuNPs than the PEG AuNPs. Statistical analysis and detailed tests of hydrophilic and hydrophobic surfaces, with both hydrophilic and hydrophobic AFM tips, helped us to exclude the role of water adsorbed on the surfaces. We found a 100% thickness increase of the 1.5 nm thick dimannoside ligand shell, hence 1.5 nm of water, corresponding to about four layers of water. The water can be absorbed in a layer, and between the various dimannose groups, absorbed.

The increased water adsorption of dimanno-AuNPs, compared to the well-studied PEG AuNPs, makes them candidates for gas sensing applications. Sensors are usually kept dry and then become hydrated in standard environments. Whenever dry conditions are problematic, our study suggests testing carbohydrate coatings.

Finally, revealing the water adsorption of dimannoside from dryness to high humidity offers new insights into the molecular role of these surface residues also from a biophysical perspective, which is especially valuable when the biological objects in question are highly pathogenic. Size, surface composition, and controlled orientation of the dimanno-AuNPs suggest suitable candidates for emulating viral surface glycoproteins -like influenza hemagglutinin- under hydration-dehydration cycles in air, which correspond to the conditions of viral transmission. Indeed, several viral pathogens display mannose residues on their surface, particularly surface glycoproteins. These are responsible for infection, but might also provide adaptability to harsh environments, such as dry conditions. Our approach is yet focused exclusively on water; future investigations should include the effects of adsorbed salts and proteins, and the temperature.

Experimental Part

Materials

Acetone (99.5 %), 3-(ethoxy-dimethylsilyl) propylamine (APDMES, 97 %), and anhydrous solutions of toluene, chloroform, octadecyl trichlorosilane (OTS), and decalin cis+trans were purchased from Sigma Aldrich (Germany). 2-propanol (99.5 %) was obtained from Acros (Belgium) and absolute ethanol (99 %) from Panreac (Spain). Dimanno-AuNPs and PEG AuNPs aqueous solutions were kindly provided by the Bio Nano Plasmonics Lab at CIC Biomagune (San Sebastián, Spain). Water was of ultrapure quality (Milli-Q, 18.2 M Ω cm, <10 ppb total organic content).

Synthesis of gold nanoparticles

Gold nanoparticles were synthesized by the Bio Nano Plasmonics Lab at CIC biomaGUNE according to [10]. Both PEG AuNPs and dimanno-AuNPs were obtained by reduction of AuCl₄⁻ with BH₄⁻ in the presence of the corresponding thiol ligands. For the PEG AuNPs, a PEG thiol with carboxylic acid termination was used. To obtain the dimanno-AuNPs, 50 mol% of the same carboxylic acid ligand was mixed with 50 mol% of a dimannoside (Man α 1-2Man) thiourea PEG thiol. After purification and lyophilization, the nanoparticles were obtained as brown powders.

Dynamic light scattering (DLS) and zeta potential (ZP) measurements

DLS was used to determine the hydrodynamic diameter, and ZP was used to estimate the NP surface charge of both particles in solution. We employed Zetasizer Nano ZS (Malvern Panalytical, UK) equipment. For DLS measurements, 70 μ L of the sample (1.0×10^{12} particles/mL) was loaded in a previously Milli Q washed micro-cuvette at 25 °C and a detection angle of 173°. For ZP, 700 μ L of the sample was loaded in a dip-cell cuvette. Three runs were performed in three replicates, resulting in nine

measurements per sample. The hydrodynamic diameter (z average) and the NP surface charge (ZP) were calculated with the equipment software (v.7.12) without any further data processing, hence assuming spherical shapes. For ZP, we set the factor $f(Ka)=1.5$ and used the Smoluchowski approximation.

Preparation of hydrophilic and hydrophobic surfaces

Dimanno-AuNPs and PEG AuNPs were adsorbed on silicon wafers which we functionalized with APDMES or with OTS (see Supp. Info. S1), referred to as "hydrophilic" or "hydrophobic", respectively. The silicon wafers were initially chemically cleaned by successive serial sonication steps of 5 minutes each using acetone, 2-propanol and absolute ethanol and then dried with a nitrogen stream. Oxygen plasma etching (Diener, DE) was carried out for 8 minutes with 300 W of nominal power (100 %), at mbar oxygen pressure, which creates an OH-terminated layer of hydrophilic silicon oxide.

For the hydrophilic functionalization, the surfaces were subsequently immersed in 2 mL of APDMES in toluene (1:100 v/v) and heated to 60 °C for 30 minutes. To avoid the hydrolyzation of the APDMES, the procedure was achieved in a glove box. After functionalization, the surfaces were rinsed in toluene and dried in flowing nitrogen.

The hydrophobic functionalization was performed as reported in [24]. Silicon wafers were washed first in methanol, then in a 1:1 v/v mixture of methanol and chloroform, and finally in chloroform under 5 min sonication at every step. Afterwards, the surfaces were immersed in a 7:2:1 v/v mixture of decalin cis+trans/toluene/chloroform and 0.1 % OTS was added. The procedure was done at ambient temperature inside a nitrogen glove box. After 12 hours of incubation, the surfaces were rinsed with chloroform, then with a 1:1 v/v mixture of chloroform and methanol, and finally with methanol. The process was finished by drying the surfaces with a stream of nitrogen.

Contact angle measurements

For static contact angle measurements, sessile drop experiments were performed in triplicates at ambient temperature (23-25 °C) with a standard contact-angle measurement system (G10 goniometer, Krüss). A droplet of ultrapure water of volume 4 μ L was placed onto the functionalized silicon surfaces and contact angles from the drop profile were measured.

Adsorption of nanoparticles

Dimanno-AuNPs or PEG AuNPs solutions were incubated for 5 min (1.0×10^{12} particles/mL) on the hydrophilic functionalized silicon surfaces. The samples were washed with Milli Q water and dried in flowing nitrogen. The adsorption on the hydrophobic surfaces was achieved by drop casting. A droplet of dimanno-AuNPs or PEG AuNPs was deposited on the surface and dried in air.

Infrared spectroscopy

FTIR measurements were carried out with a grazing incidence objective lens/mirror system in a Hyperion 2000 microscope with a Vertex 70 spectrometer (Bruker). For this, a concentrated solution of particles (1.9×10^{13} particles/mL) was cast on a carefully cleaned gold surface and evaporated under ambient conditions. The measurements were achieved by recording 2000 scans, from 650 to 4000 cm^{-1} and a resolution of 4 cm^{-1} , in triplicate. Background spectra were recorded on gold areas outside the evaporated droplet. The FTIR spectra were obtained with the equipment software OPUS v.6.5 without further data processing.

Sum frequency generation spectroscopy

VSFG spectra of dimanno-AuNPs and PEG AuNPs was recorded in a broad-band VSFG system at Fritz Haber Institute. Gold thin films (200 nm on 10 nm Cr on glass) were used as surfaces. Previously to sample deposition, the surfaces were cleaned with ethanol, and Milli Q water under sonication for 10 minutes. UV/ozone cleaning was applied to remove any possible hydrocarbon contamination, and the VSFG spectra of the washed gold was used as reference to normalize the non-flat infrared power distribution, similar to FTIR recording. About 10 μL of the sample was drop cast on the surface and evaporated under nitrogen flow. The VSFG experiments were achieved under dry air flushing at room temperature (24 °C) at 4 different center frequencies to measure the complete CH and OH stretching region in the broad band infrared. The tunable infrared laser produced femtosecond pulses of ~5.5 mW (at 3300 cm^{-1}). Their focus length was 30 cm and the incident angle 45°. The visible picosecond pulses were at a fixed frequency of 800 nm (12500 cm^{-1}), and of 10 mW power. Their focus length was 100 cm and the incident angle 65°. The sum frequency signal was collected in reflection, accumulated for 1 min for ppp polarization (all beams polarized normal to the surface) and 2 min for ssp (laser beams polarized parallel to the surface, sum frequency emission and up-conversion polarized perpendicular and infrared parallel to the plane of incidence).

Electron microscope imaging

SEM and STEM images were obtained in a Helios NanoLab 450S dual beam microscope (FEI NL / Thermo Fisher Scientific). SEM images were obtained of dimanno-AuNPs and PEG AuNPs at 5 kV with 50 pA current in high vacuum mode. The core diameter of single particles was manually counted with ImageJ (NIH, <https://imagej.nih.gov/ij/>). The number of particles was expressed as "n" and the data were displayed as the mean \pm SD. A total of 378 particles were counted for the dimanno-AuNPs and 491 for the PEG AuNPs.

STEM acquisition was achieved in high vacuum at 30 keV, 50 pA current on negatively stained dimanno-AuNPs samples. For the negative staining, 0.35 μL of dimanno-AuNPs (1.9×10^{13} particles/mL) were deposited on glow discharged carbon TEM grids (air flow, 20 mA, 4 minutes). Then, 0.35 μL uranyl acetate (0.5 % w/w) was deposited and dried on the sample.

AFM imaging

AFM topography images were recorded with an Agilent 5500 AFM (Keysight, Scientec, FR), in air in AC “noncontact” mode at 24 °C, at speed between 0.8 and 1.2 lines/s. The scanning was performed in at least six replicates per condition for the PEG AuNPs and nine replicates for the dimanno-AuNPs.

Silicon cantilevers (Multi 75, Budget Sensors) with a force constant (k) of 3 N/m, a resonance frequency (f) of 75 kHz and a nominal radius of <10 nm were used for the experiments on the hydrophilic surfaces. These conditions are referred to as “hydrophilic conditions”.

The visualization of particles on hydrophobic surfaces was achieved by employing gold-coated silicon probes with a 1 nm carbon spike (k 5 N/m, f 160 kHz, HiRes C14 /Cr Au, MikroMasch). These conditions are referred to as “hydrophobic conditions”.

The samples were incubated on the hydrophilic or hydrophobic surfaces, and AFM topography images were taken under humidity-controlled atmospheres at (15 ± 5) %, (50 ± 5) % and (90 ± 5) % of RH. These humidity conditions are referred to as “low humidity”, “medium humidity” and “high humidity”, respectively. For this, an environmental isolation chamber (Keysight) was mounted to the AFM, thus providing a completely sealed and isolated environment. The RH of (15 ± 5) % was achieved by pumping nitrogen to the isolation chamber. The RH of (50 ± 5) % was reached by controlling the mixing ratio between a dry and a wet stream of nitrogen, produced in a bubble flask. To reach RH of (90 ± 5) %, the sample was allowed to equilibrate overnight in the saturated chamber. The images were examined by using picoView 1.14 software (Keysight). AFM images were analyzed after scanning with WSxM 5.0 Develop software version 8.0 [46] for obtaining the maximum height of the particles and height profiles. For this, the images were processed by levelling the plane of the image and applying parabolic flattening. Around 500 individual particles were processed in the hydrophilic conditions and 250 in the hydrophobic conditions. The particles were manually selected by using the criterion of single particle observation with a FWHM below 30 nm and 40 nm for the hydrophilic and hydrophobic conditions, respectively. Gwyddion software version 2.47 was used for displaying the topography images. The images were first levelled by mean plane subtraction, aligned by height median and occasionally, the z excursions outliers were manually removed by, e.g. correction of the scan line artefacts in the x axis or misaligned segments within a single row. The height distribution histograms were calculated with Origin 8.0 software and height profiles were obtained with GraphPad Prism version 8.0.1. The number of particles was expressed as “n” and the data were displayed as the mean ± SD.

Statistical Analysis

Statistical analysis was performed using GraphPad Prism version 8.0.1. Data sets were analyzed using unpaired t-tests (Mann-Whitney test) to compare identical particles on different surfaces at the same humidity. Two-tailed P values were reported in all the cases, and the alpha level was kept at 0.05.

Acknowledgements

The presented results are partially based on Maiara Iriarte-Alonso’s PhD thesis “Surface models of Influenza virus envelope: Biophysical studies under various

hydration scenarios”, University of the Basque Country (2022). We thank Isabel Garcia (CIC biomaGUNE, Donostia-San Sebastián, Spain) for the synthesis of the particles. AMB acknowledges the Erwin Schrödinger Institute (ESI) for Mathematics and Physics in Wien, Austria. We are grateful for funding by grants EU-MSCA 101072645 nanoremedi, EIC-pathfinder 101115292 (“textadna”), the Spanish MINECO for the Maria de Maeztu Units of Excellence Program (CEX2020-001038-M/MCIN/AEI/10.13039/501100011033), and for the projects PID2019-104650GB-C22 (Bridge), PID2023-147987OB-C32, PID2023-146348NB-I00; the Basque Government for the Elkartek ng; the Diputacion Foral Gipuzkoa for the project “shifte”. MAIA received an EMBO and a DAAD travel grant that allowed her to work at FHI Berlin. We thank the electron microscopy group at CIC nanoGUNE for advice and help.

References

[1] S. Balci, K. Noda, A.M. Bittner, A. Kadri, C. Wege, H. Jeske, K. Kern, Self-Assembly of Metal-Virus Nanodumbbells. *Angew. Chemie Int. Ed.* 46 (2007) 3149-3151

<https://doi.org/10.1002/anie.200604558>

[2] F. Compostella, O. Pitirollo, A. Silvestri, L. Polito, Glyco-gold nanoparticles: synthesis and applications. *Beilstein J. Org. Chem.* 2017, 13, 1008–1021

<https://doi.org/10.3762/bjoc.13.100>

[3] G.A.Kausche, H. Ruska, Die Sichtbarmachung der Adsorption von Metallkolloiden an Eiweisskörper. *Kolloid-Zeitschrift* 89 (1939) 21-26

<https://doi.org/10.1007/BF01518802>

[4] A.M. Alkilany, C.J. Murphy, Toxicity and cellular uptake of gold nanoparticles: What we have learned so far? *J. Nanoparticle Res.* 12 (2010) 2313–2333

<https://doi.org/10.1007/s11051-010-9911-8>

[5] B.C. Dhar, Diagnostic assay and technology advancement for detecting SARS-CoV-2 infections causing the COVID-19 pandemic. *Anal. Bioanal. Chem.* 414 (2022) 2903–2934

<https://doi.org/10.1007/s00216-022-03918-7>

[6] N. Climent, I. García, M. Marradi, F. Chiodo, L. Miralles, M.J. Maleno, J.M. Gatell, F. García, S. Penadés, M. Plana, Loading dendritic cells with gold nanoparticles (GNPs) bearing HIV-peptides and mannosides enhance HIV-specific T cell responses, *Nanomedicine Nanotechnology. Biol. Med.* 14 (2018) 339–351

<https://doi.org/10.1016/j.nano.2017.11.009>

[7] G. Sonavane, K. Tomoda, K. Makino, Biodistribution of colloidal gold nanoparticles after intravenous administration: Effect of particle size. *Colloids Surfaces B Biointerfaces.* 66 (2008) 274–280

<https://doi.org/10.1016/j.colsurfb.2008.07.004>

[8] K.D. McReynolds, M.J. Hadd, J. Gervay-Hague, Synthesis of biotinylated glycoconjugates and their use in a novel ELISA for direct comparison of HIV-1 gp120 recognition of GalCer and related carbohydrate analogues. *Bioconjug. Chem.* 10 (1999) 1021–1031

<https://doi.org/10.1021/bc990050x>

[9] C.N. Scanlan, J. Offer, N. Zitzmann, R.A. Dwek, Exploiting the defensive sugars of HIV-1 for drug and vaccine design. *Nature.* 446 (2007) 1038–1045
<https://doi.org/10.1038/nature05818>

[10] O. Martínez-Ávila, K. Hijazi, M. Marradi, C. Clavel, C. Campion, C. Kelly, S. Penadés, Gold Manno-Glyconanoparticles: Multivalent systems to block HIV-1 gp120 binding to the lectin DC-SIGN. *Chem. - A Eur. J.* 15 (2009) 9874–9888

<https://doi.org/10.1002/chem.200900923>

[11] J. Pan, N.K. Duggal, S.S. Lakdawala, N.C. Rockey, L.C. Marr, Mucin Colocalizes with Influenza Virus and Preserves Infectivity in Deposited Model Respiratory Droplets. *Environ. Sci. Technol.* 59 (2025) 2192-2200

<https://doi.org/10.1021/acs.est.4c10886>

[12] A.K. Longest, N.C. Rockey, S.S. Lakdawala, L.C. Marr, Review of factors affecting virus inactivation in aerosols and droplets. *J. R. Soc. Interface* 21 (2024) 20240018

<https://doi.org/10.1098/rsif.2024.0018>

[13] J.L. Kyle, E. Harris, Global spread and persistence of dengue. *Annu. Rev. Microbiol.* 62 (2008) 71–92

<https://doi.org/10.1146/annurev.micro.62.081307.163005>

[14] S. Ng, N.E. Basta, B.J. Cowling, Association between temperature, Humidity and ebolavirus disease outbreaks in Africa, 1976 to 2014. *Eurosurveillance* 19 (2014) 1–11

<https://doi.org/10.2807/1560-7917.es2014.19.35.20892>

[15] N.H.L. Leung, Transmissibility and transmission of respiratory viruses. *Nat. Rev. Microbiol.* 19 (2021) 528–545

<https://doi.org/10.1038/s41579-021-00535-6>

[16] W. Weissenhorn, A. Dessen, L.J. Calder, S.C. Harrison, J.J. Skehel, D.C. Wiley, Structural basis for membrane fusion by enveloped viruses. *Mol. Membr. Biol.* 16 (1999) 3–9

<https://doi.org/10.1080/096876899294706>

[17] H.K. Abeyratne-Perera, P.L. Chandran, Mannose Surfaces Exhibit Self-Latching, Water Structuring, and Resilience to Chaotropes: Implications for Pathogen Virulence. *Langmuir* 33 (2017) 9178–9189

<https://doi.org/10.1021/acs.langmuir.7b01006>

[18] M.A. Iriarte-Alonso, A.M. Bittner, S. Chiantia, Influenza A virus hemagglutinin prevents extensive membrane damage upon dehydration. *BBA Adv.* 2 (2022) 100048

<https://doi.org/10.1016/j.bbadv.2022.100048>

[19] G. Katz, Y. Benkarroum, H. Wei, W.J. Rice, D. Bucher, A. Alimova, A. Katz, J. Klukowska, G.T. Herman, P. Gottlieb, Morphology of Influenza B/Lee/40 Determined by Cryo-Electron Microscopy. *PLoS ONE* 9 (2014) e88288

<https://doi.org/10.1371/journal.pone.0088288>

[20] A. Calò, A. Eleta-Lopez, T. Ondarçuhu, A. Verdaguer, A.M. Bittner, Nanoscale wetting of single viruses. *Molecules.* 26 (2021) 1–11

<https://doi.org/10.3390/molecules26175184>

- [21] A. Verdager, G.M. Sacha, H. Bluhm, M. Salmeron, Molecular Structure of Water at Interfaces: Wetting at the Nanometer Scale. *Chem. Rev.*, 106 (2006) 1478-1510
- [22] S. Santos, C.A. Amadei, C.Y. Lai, T. Olukan, J.Y. Lu, J. Font, V. Barcons, A. Verdager, M. Chiesa, Investigating the Ubiquitous Presence of Nanometric Water Films on Surfaces. *J. Phys. Chem. C*, 125 (2021) 15759-15772
<https://doi.org/10.1021/acs.jpcc.1c03767>
- [23] S. Santos, A. Verdager, T. Souier, N.H. Thomson, M. Chiesa, Measuring the true height of water films on surfaces. *Nanotechnology*. 22 (2011)
<https://doi.org/10.1088/0957-4484/22/46/465705>
- [24] A.E. Lopez, S. Moreno-Flores, D. Pum, U.B. Sleytr, J.L. Toca-Herrera, Surface dependence of protein nanocrystal formation. *Small*. 6 (2010) 396–403
<https://doi.org/10.1002/smll.200901169>
- [25] J.R. Harris, *Negative Staining of Thinly Spread Biological Particulates*. Humana Press, 1999
<https://doi.org/https://doi.org/10.1385/1-59259-201-5:13>
- [26] Y. Tong, E. Tyrode, M. Osawa, N. Yoshida, T. Watanabe, A. Nakajima, S. Ye, Preferential Adsorption of Amino-Terminated Silane in a Binary Mixed Self-Assembled Monolayer. *Langmuir* 27 (2011) 5420–5426
<https://doi.org/10.1021/la200497u>
- [27] R.N. Ward, P.B. Davies, C.D. Bain, Orientation of surfactants adsorbed on a hydrophobic surface. *J. Phys. Chem.* 97 (1993) 7141-7143
<https://doi.org/10.1021/j100130a005>
- [28] D.E. Gragson, B.M. McCarty, G.L. Richmond, Surfactant/Water Interactions at the Air/Water Interface Probed by Vibrational Sum Frequency Generation. *J. Phys. Chem.* 100 (1996) 14272-14275
<https://doi.org/10.1021/jp961034p>
- [29] M.U.A. Ahlqvist, L.S. Taylor, Water diffusion in hydrated crystalline and amorphous sugars monitored using H/D exchange. *J. Pharm. Sci.* 91 (2002) 690–698
<https://doi.org/10.1002/jps.10068>
- [30] A. Eleta-Lopez, A. Calò, Key factors of scanning a plant virus with AFM in air and aqueous solution. *Microsc. Res. Tech.* 80 (2017) 18–29
<https://doi.org/10.1002/jemt.22741>
- [31] X. Shen, C.-M. Ho, T.-S. Wong, Minimal Size of Coffee Ring Structure. *J Phys Chem B*. 114 (2010) 5269–5274
<https://doi.org/doi:10.1021/jp912190v>
- [32] C. Kunstmann-Olsen, D. Belić, D.F. Bradley, M.P. Grzelczak, M. Brust. Humidity-Dependent Reversible Transitions in Gold Nanoparticle Superlattices, *Chem. Mater.* 28 (2016) 2970–2980

<https://doi.org/10.1021/acs.chemmater.6b00070>

[33] L. Zitzler, S. Herminghaus, F. Mugele, Capillary forces in tapping mode atomic force microscopy. *Phys. Rev. B - Condens. Matter Mater. Phys.* 66 (2002) 1–8
<https://doi.org/10.1103/PhysRevB.66.155436>

[34] A.E. López, D. Pum, U.B. Sleytr, J.L. Toca-Herrera, Influence of surface chemistry and protein concentration on the adsorption rate and S-layer crystal formation. *Phys. Chem. Chem. Phys.* 13 (2011) 11905–11913
<https://doi.org/10.1039/c1cp00052g>

[35] M. Cascajo-Castresana, R.O. David, M.A. Iriarte-Alonso, A.M. Bittner, C. Marcolli, Protein aggregates nucleate ice: The example of apoferritin. *Atmos. Chem. Phys.* 20 (2020) 3291–3315

<https://doi.org/10.5194/acp-20-3291-2020>

[36] J.H. Melillo, J.P. Gabriel, F. Pabst, T. Blochowicz, S. Cervený, Dynamics of aqueous peptide solutions in folded and disordered states examined by dynamic light scattering and dielectric spectroscopy. *Phys. Chem. Chem. Phys.* 23 (2021) 15020–15029

<https://doi.org/10.1039/d1cp01893k>

[37] L.F. Leopold, I.S. Tódor, Z. Diaconeasa, D. Rugină, A. Ștefancu, N. Leopold, C. Coman, Assessment of PEG and BSA-PEG gold nanoparticles cellular interaction. *Colloids Surfaces A Physicochem. Eng. Asp.* 532 (2017) 70–76

<https://doi.org/10.1016/j.colsurfa.2017.06.061>

[38] K.K. Katti, V. Kattumuri, S. Bhaskaran, K. V. Katti, R. Kannan, Facile and general method for synthesis of sugar-coated gold nanoparticles. *Int. J. Green Nanotechnol. Biomed.* 1 (2009) 1–8

<https://doi.org/10.1080/19430850902983848>

[39] N. Leopold, V. Chiș, N.E. Mircescu, O.T. Marișca, O.M. Buja, L.F. Leopold, C. Socaciu, C. Braicu, A. Irimie, I. Berindan-Neagoe, One step synthesis of SERS active colloidal gold nanoparticles by reduction with polyethylene glycol. *Colloids Surfaces A Physicochem. Eng. Asp.* 436 (2013) 133–138

<https://doi.org/10.1016/j.colsurfa.2013.05.075>

[40] K. Kobayashi, N. Oyabu, K. Kimura, S. Ido, K. Suzuki, T. Imai, K. Tagami, M. Tsukada, H. Yamada, Visualization of hydration layers on muscovite mica in aqueous solution by frequency-modulation atomic force microscopy. *J. Chem. Phys.* 138 (2013)

<https://doi.org/10.1063/1.4803742>

[41] C.K. Madawala, H.D. Lee, C.P. Kaluarachchi, A.V. Tivanski, Probing the Water Uptake and Phase State of Individual Sucrose Nanoparticles Using Atomic Force Microscopy. *ACS Earth Space Chem.* 5 (2021), 2612–2620

<https://doi.org/10.1021/acsearthspacechem.1c00101>

[42] T. Fukuma, R. Garcia, Atomic- and Molecular-Resolution Mapping of Solid-Liquid Interfaces by 3D Atomic Force Microscopy. *ACS Nano.* 12 (2018) 11785–11797

<https://doi.org/10.1021/acsnano.8b07216>

[43] O. Björneholm, M.H. Hansen, A. Hodgson, L.-M. Liu, D.T. Limmer, A. Michaelides, P. Pedevilla, J. Rossmeisl, H. Shen, G. Tocci, E. Tyrode, M.-M. Walz, J. Werner, H. Bluhm, *Water at Interfaces. Chem. Rev.* 116 (2016), 7698-7726

<https://doi.org/10.1021/acs.chemrev.6b00045>

[44] D. Reishofer, R. Resel, J. Sattelkow, W.J. Fischer, K. Niegelhell, T. Mohan, K.S. Kleinschek, H. Amenitsch, H. Plank, T. Tammelin, E. Kontturi, S. Spirk, *Humidity Response of Cellulose Thin Films. Biomacromolecules* 23 (2022), 1148-1157

<https://doi.org/10.1021/acs.biomac.1c01446>

[45] C. Kunstmann-Olsen, D. Belić, M. Brust, *Monitoring pattern formation in drying and wetting dispersions of gold nanoparticles by ESEM. Faraday Discuss.* 181 (2015) 281–298

<https://doi.org/10.1039/c4fd00270a>

[46] I. Horcas, R. Fernandez, *WSXM: A software for scanning probe microscopy and a tool for nanotechnology. Rev. Sci. Instrum.* 78 (2007) 013705

<https://doi.org/10.1063/1.2432410>